Research Article | Vol. 25, No. 4 | 20 Feb 2017 | OPTICS EXPRESS 3863

Optics EXPRESS

Meta-nanocavity model for dynamic super-resolution fluorescent imaging based on the plasmonic structure illumination microscopy method

SHUN CAO,[1,2] TAISHENG WANG,[1] QIANG SUN,[1] BINGLIANG HU,[3] AND WEIXING YU[3,*]

[1] *State Key Laboratory of Applied Optics, Changchun Institute of Optics, Fine Mechanics & Physics, Chinese Academy of Sciences, No.3888, Dongnanhu Road, Changchun, Jilin, China*
[2] *University of the Chinese Academy of Sciences, Beijing, 10039, China*
[3] *Key Laboratory of Spectral Imaging Technology, Xi'an Institute of Optics and Precision Mechanics, Chinese Academy of Sciences, No.17, Xinxi Road, Xian 710119, China*
[*] *yuwx@opt.ac.cn*

Abstract: Biological research requires dynamic and wide-field optical microscopy with resolution down to nanometer to study the biological process in a sub-cell or single molecular level. To address this issue, we propose a dynamic wide-field optical nanoimaging method based on a meta-nanocavity platform (MNCP) model which can be incorporated in micro/nano-fluidic systems so that the samples to be observed can be confined in a nano-scale space for the ease of imaging. It is found that this platform can support standing wave surface plasmons (SW-SPs) interference pattern with a period of 105 nm for a 532 nm incident wavelength. Furthermore, the potential application of the NCP for wide-field super-resolution imaging was discussed and the simulation results show that an imaging resolution of sub-80 nm can be achieved.

OCIS codes: (100.6640) Superresolution; (160.3918) Metamaterials; (180.2520) Fluorescence microscopy; (240.6680) Surface plasmons.

References and links

1. E. A. Ash and G. Nicholls, "Super-resolution aperture scanning microscope," Nature **237**(5357), 510–512 (1972).
2. Z. Liu, S. Durant, H. Lee, Y. Pikus, N. Fang, Y. Xiong, C. Sun, and X. Zhang, "Far-field optical superlens," Nano Lett. **7**(2), 403–408 (2007).
3. Y. Xiong, Z. Liu, C. Sun, and X. Zhang, "Two-dimensional imaging by far-field superlens at visible wavelengths," Nano Lett. **7**(11), 3360–3365 (2007).
4. S. W. Hell and J. Wichmann, "Breaking the diffraction resolution limit by stimulated emission: stimulated-emission-depletion fluorescence microscopy," Opt. Lett. **19**(11), 780–782 (1994).
5. X. Yang, H. Xie, E. Alonas, Y. Liu, X. Chen, P. J. Santangelo, Q. Ren, P. Xi, and D. Jin, "Mirror-enhanced super-resolution microscopy," Light Sci. Appl. **5**(6), e16134 (2016).
6. E. Betzig, G. H. Patterson, R. Sougrat, O. W. Lindwasser, S. Olenych, J. S. Bonifacino, M. W. Davidson, J. Lippincott-Schwartz, and H. F. Hess, "Imaging intracellular fluorescent proteins at nanometer resolution," Science **313**(5793), 1642–1645 (2006).
7. M. G. L. Gustafsson, "Surpassing the lateral resolution limit by a factor of two using structured illumination microscopy," J. Microsc. **198**(2), 82–87 (2000).
8. Z. Liu, H. Lee, Y. Xiong, C. Sun, and X. Zhang, "Far-field optical hyperlens magnifying sub-diffraction-limited objects," Science **315**(5819), 1686 (2007).
9. J. N. Anker, W. P. Hall, O. Lyandres, N. C. Shah, J. Zhao, and R. P. Van Duyne, "Biosensing with plasmonic nanosensors," Nat. Mater. **7**(6), 442–453 (2008).
10. S. I. Bozhevolnyi, V. S. Volkov, E. Devaux, J. Y. Laluet, and T. W. Ebbesen, "Channel plasmon subwavelength waveguide components including interferometers and ring resonators," Nature **440**(7083), 508–511 (2006).
11. X. Hao, C. Kuang, Z. Gu, Y. Wang, S. Li, Y. Ku, Y. Li, J. Ge, and X. Liu, "From microscopy to nanoscopy via visible light," Light Sci. Appl. **2**(10), e108 (2013).
12. N. Li, A. Tittl, S. Yue, H. Giessen, C. Song, B. Ding, and N. Liu, "DNA-assembled bimetallic plasmonic nanosensors," Light Sci. Appl. **3**(12), e226 (2014).

#280511 https://doi.org/10.1364/OE.25.003863
Journal © 2017 Received 10 Nov 2016; revised 19 Jan 2017; accepted 6 Feb 2017; published 14 Feb 2017

13. Z. Liu, J. M. Steele, W. Srituravanich, Y. Pikus, C. Sun, and X. Zhang, "Focusing surface plasmons with a plasmonic lens," Nano Lett. **5**(9), 1726–1729 (2005).
14. N. Fang, H. Lee, C. Sun, and X. Zhang, "Sub-diffraction-limited optical imaging with a silver superlens," Science **308**(5721), 534–537 (2005).
15. J. B. Pendry, "Negative refraction makes a perfect lens," Phys. Rev. Lett. **85**(18), 3966–3969 (2000).
16. X. Zhang and Z. Liu, "Superlenses to overcome the diffraction limit," Nat. Mater. **7**(6), 435–441 (2008).
17. E. Chung, Y.-H. Kim, W. T. Tang, C. J. R. Sheppard, and P. T. C. So, "Wide-field extended-resolution fluorescence microscopy with standing surface-plasmon-resonance waves," Opt. Lett. **34**(15), 2366–2368 (2009).
18. P. S. Tan, X. C. Yuan, G. H. Yuan, and Q. Wang, "High-resolution wide-field standing-wave surface plasmon resonance fluorescence microscopy with optical vortices," Appl. Phys. Lett. **97**(24), 241109 (2010).
19. Q. Wang, J. Bu, P. S. Tan, G. H. Yuan, J. H. Teng, H. Wang, and X.-C. Yuan, "Subwavelength-sized plasmonic structures for wide-field optical microscopic imaging with super-resolution," Plasmonics **7**(3), 427–433 (2012).
20. F. Wei and Z. Liu, "Plasmonic structured illumination microscopy," Nano Lett. **10**(7), 2531–2536 (2010).
21. F. Wei, D. Lu, H. Shen, W. Wan, J. L. Ponsetto, E. Huang, and Z. Liu, "Wide field super-resolution surface imaging through plasmonic structured illumination microscopy," Nano Lett. **14**(8), 4634–4639 (2014).
22. B. Gjonaj, A. David, Y. Blau, G. Spektor, M. Orenstein, S. Dolev, and G. Bartal, "Sub-100 nm focusing of short wavelength plasmons in homogeneous 2D space," Nano Lett. **14**(10), 5598–5602 (2014).
23. P. A. Belov and Y. Hao, "Subwavelength imaging at optical frequencies using a transmission device formed by a periodic layered metal-dielectric structure operating in the canalization regime," Phys. Rev. B **73**(11), 113110 (2006).
24. W. L. Gao, F. Z. Fang, Y. M. Liu, and S. Zhang, "Chiral surface waves supported by biaxial hyperbolic metamaterials," Light Sci. Appl. **4**(9), e328 (2015).
25. Y. Xiong, Z. Liu, and X. Zhang, "Projecting deep-subwavelength patterns from diffraction-limited masks using metal-dielectric multilayers," Appl. Phys. Lett. **93**(11), 111116 (2008).
26. S. Cao, T. Wang, W. Xu, H. Liu, H. Zhang, B. Hu, and W. Yu, "Gradient permittivity meta-structure model for wide-field super-resolution imaging with a sub-45 nm resolution," Sci. Rep. **6**, 23460 (2016).
27. G. M. Whitesides, "The origins and the future of microfluidics," Nature **442**(7101), 368–373 (2006).
28. X. Cui, L. M. Lee, X. Heng, W. Zhong, P. W. Sternberg, D. Psaltis, and C. Yang, "Lensless high-resolution on-chip optofluidic microscopes for Caenorhabditis elegans and cell imaging," Proc. Natl. Acad. Sci. U.S.A. **105**(31), 10670–10675 (2008).
29. X. Cui, M. Lew, and C. Yang, "Quantitative differential interference contrast microscopy based on structured-aperture interference," Appl. Phys. Lett. **93**(9), 091113 (2008).
30. X. Heng, D. Erickson, L. R. Baugh, Z. Yaqoob, P. W. Sternberg, D. Psaltis, and C. Yang, "Optofluidic microscopy--a method for implementing a high resolution optical microscope on a chip," Lab Chip **6**(10), 1274–1276 (2006).
31. X. Fang, K. F. MacDonald, and N. I. Zheludev, "Controlling light with light using coherent metadevices: all-optical transistor, summator and invertor," Light Sci. Appl. **4**, e292 (2015).
32. W. Sun, Q. He, S. Sun, and L. Zhou, "High-efficiency surface plasmon meta-couplers: concept and microwave-regime realizations," Light Sci. Appl. **5**(1), e16003 (2016).
33. P. B. Johnson and R. W. Christy, "Optical constants of the noble metals," Phys. Rev. B **6**(12), 4370–4379 (1972).
34. H. T. Miyazaki and Y. Kurokawa, "Squeezing visible light waves into a 3-nm-thick and 55-nm-long plasmon cavity," Phys. Rev. Lett. **96**(9), 097401 (2006).
35. E. Verhagen, J. A. Dionne, L. K. Kuipers, H. A. Atwater, and A. Polman, "Near-field visualization of strongly confined surface plasmon polaritons in metal-insulator-metal waveguides," Nano Lett. **8**(9), 2925–2929 (2008).
36. H. Raether, *Surface Plasmons on Smooth and Rough Surfaces and Gratings* (Springer Berlin Heidelberg, 1988).
37. M. Papaioannou, E. Plum, J. Valente, E. T. F. Rogers, and N. I. Zheludev, "Two-dimensional control of light with light on metasurfaces," Light Sci. Appl. **5**(4), e16070 (2016).
38. Y. Zhang, H. Wang, H. Liao, Z. Li, C. Sun, J. Chen, and Q. Gong, "Unidirectional launching of surface plasmons at the subwavelength scale," Appl. Phys. Lett. **105**(23), 231101 (2014).
39. A. Pors, M. G. Nielsen, T. Bernardin, J. C. Weeber, and S. I. Bozhevolnyi, "Efficient unidirectional polarization-controlled excitation of surface plasmon polaritons," Light Sci. Appl. **3**(8), e197 (2014).
40. D. Lu, J. Kan, E. E. Fullerton, and Z. Liu, "Tunable surface plasmon polaritons in Ag composite films by adding dielectrics or semiconductors," Appl. Phys. Lett. **98**(24), 243114 (2011).
41. N. Calander, "Theory and simulation of surface plasmon-coupled directional emission from fluorophores at planar structures," Anal. Chem. **76**(8), 2168–2173 (2004).
42. N. Calander, "Surface plasmon-coupled emission and Fabry-Perot resonance in the sample layer: A theoretical approach," J. Phys. Chem. B **109**(29), 13957–13963 (2005).
43. Z. Liu, J. M. Steele, H. Lee, and X. Zhang, "Tuning the focus of a plasmonic lens by the incident angle," Appl. Phys. Lett. **88**(17), 171108 (2006).
44. P. T. So, H. S. Kwon, and C. Y. Dong, "Resolution enhancement in standing-wave total internal reflection microscopy: a point-spread-function engineering approach," J. Opt. Soc. Am. A **18**(11), 2833–2845 (2001).
45. P. E. Hänninen, S. W. Hell, J. Salo, E. Soini, and C. Cremer, "Two-photon excitation 4Pi confocal microscope: enhanced axial resolution microscope for biological research," Appl. Phys. Lett. **66**(13), 1698–1700 (1995).

46. S. Hell and E. H. K. Stelzer, "Properties of a 4Pi confocal fluorescence microscope," J. Opt. Soc. Am. A **9**(12), 2159 (1992).
47. L. Shao, B. Isaac, S. Uzawa, D. A. Agard, J. W. Sedat, and M. G. Gustafsson, "I5S: wide-field light microscopy with 100-nm-scale resolution in three dimensions," Biophys. J. **94**(12), 4971–4983 (2008).

1. Introduction

Optical microscopy always plays an important role in biological research especially for imaging living cells. However, the resolution of conventional optical microscopy is basically limited by Abbe limit to $\lambda/2\mathrm{NA}$, where λ is the wavelength of the incident light and NA is the numerical aperture of the objective lens. In visible domain, this resolution limit is about 200 nm in horizontal dimension. However, increasing demands from biological research require optical imaging method with resolution down to nanometer to study the structure in subcellular level. To meet this requirement, various novel imaging techniques have been proposed, e.g. near-field scanning optical microscopy (NSOM) [1], the far-field superlens (FSL) [2,3], stimulated emission depletion microscopy (STED) [4,5], single molecular localization techniques [6], structured illumination microscopy (SIM) [7], and the hyper-lens [8], etc. Among above methods, SIM is more suitable for high-speed vivo biological imaging due to its wide-field imaging ability. For SIM, the illumination pattern with a high spatial frequency is key to improve its resolution. More recently, surface plasmons (SPs) with intriguing properties such as strong localization and large in-plane momentum have been widely exploited for a variety of applications, such as biosensing, sub-diffraction limited imaging, and photolithography and so on [3,9–13]. SP has a higher wave-vector in comparison with the excited light in some cases and therefore is good candidate for imaging resolution improvements. At first, the super-resolution application of SPs has been extensively studied in near-field including superlens, perfect lens and hyperlens [8,14–16]. More recently, SPs were incorporated into SIM method to form the plasmonic structured illumination microscopy (PSIM) to further improve imaging resolution of SIM [17–21]. In PSIM, high resolution plasmonic interference pattern was used as the illumination pattern to achieve a lateral resolution enhancement of fluorescence image by taking advantage the higher k_{sp} of the surface plasmonic wave. A lot of efforts were dedicated to seek for higher k_{sp}, including 2D silver- silicon nitride-air platforms [22], hyperbolic metamaterials [23–25] and gradient permittivity meta-structure (GPMS) [26], etc. However, above mentioned methods have their own limitations, such as high permittivity dielectrics will restrict the interaction between biological specimen and metal film in near field [22], or the nanofabrication processes of hyperbolic metamaterials is complex and costly [23–25], or it is hard to tune the period of interference patterns in GPMS [26]. In the meantime, how to image the dynamical process in a sub-cell or single molecular level becomes very important for biological researchers to study the mass transportation or other biological process conducted in cell membrane. Recently, the advances in micro- and nano-fluidic system facilitate the dynamic detection of a single molecule [27]. Based on microfluidics, C. Yang *et al* developed a so called optofluidic microscopy (OFM) method, which is an on-chip microscopy method with high resolution and low-cost [28–30]. However, the resolution of the OFM system they can achieve is only about 1 μm, which is far away from the required nanometer-resolution.

In view of above mentioned problems, we proposed here an alternative flexible method by intelligently integrating PSIM into micro/nano-fluidic system to provide a wide-field dynamic optical imaging method with a super-resolution. In the method, a nano-cavity platform (NCP) is introduced to achieve a higher k_{sp} which is then explored for imaging resolution enhancement. The so called NCP consists of two parts with the similar structure: Ag/SiO_2. Through varying the spacing of two parts and the liquid filled in the nano-cavity, the periodic plasmonic interference patterns can be tuned very flexibly. It is found that the period of plasmonic interference pattern is 105 nm for a 532 nm incident wavelength by NCP with a 30 nm thick water-cavity. As a result, image with a resolution of 83 nm can be achieved in one dimension by employing the proposed NCP in PSIM.

2. Nano-cavity platform and simulation model description

Figure 1 shows the proposed NCP which consists of two parts. In Fig. 1(b), the bottom part (Part I) simply contains a SiO_2 layer named *Layer A* and a silver film named *Layer B*. Similarly, the SiO_2 and Ag films also form the top part (Part II) with different thickness for Ag film. After rotating the Part II with 180°and placing it upon the Part I, one form of the NCP can be obtained, i.e., the nano-air-cavity platform (NACP), as shown in Fig. 1(c). The gap between the Part I and II will affect the imaging resolution of the NACP. One can let the observed biological samples pass through the nanocavity by connecting the nanocavity with a nano-fluid system. In this case, the NACP would be changed to nano-solvent-cavity platform (NSCP). Models for both NACP and NSCP were built to simulate the standing wave surface plasmons (SW-SPs) formed in the air or solvent filled nanocavity. In NSCP, water is used to mimic the aqueous environment for biological samples. Figures 1(c) and 1(d) show the perspective sectional views of each unit cell of the NACP and NSCP, respectively. To realize wide-field imaging, the NCPs are designed in a periodic array with a period $P = 2100$ nm in both x and y directions. The thickness of the top and bottom SiO_2 layers is $d_A = d_E = 200$ nm. The bottom Ag film with a thickness of $d_B = 100$ nm is thick enough to block the incident light from propagating through the NCP. Particularly, in this layer, a SiO_2 slit with a width $W = 100$ nm in x direction and an infinite length in y direction was fabricated and used to couple the incident light into SPs. Other coupling elements such as half circle slits [22] or special designed meta-devices [31,32] can also be used to generate additional forms of SPs interference patterns. The top silver film has a thickness $d_D = 50$ nm. The material of *Layer C* (the gap) with a 30 nm thickness is air or water, functioning the object plane in the plasmonic structure illuminated microscopy.

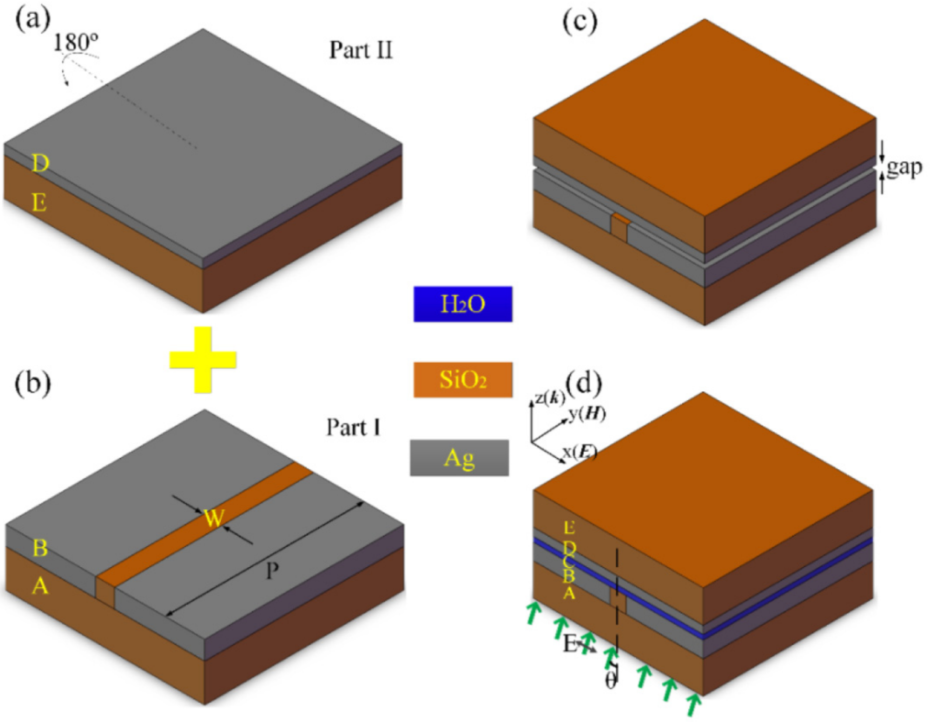

Fig. 1. The schematic diagram of the nano-cavity platform. (a) Part II, and (b) Part I, (c) schematic diagram of the nano-air-cavity platform: the combination of Part I and Part II with 180° rotation along x-axis, and (d) schematic diagram of the nano-water-cavity platform.

Both NACP and NSCP were modeled and analyzed by using the commercial-grade simulator (Lumerical Solutions, Inc.) based on the finite-difference time-domain (FDTD) method. As can be seen in Fig. 1(d), a TM polarization plane wave with $\lambda_0 = 532$ nm incident perpendicularly onto silver film in z direction with an incident angle $\theta_0 = 0$. The inset of Fig. 1(d) shows the direction of incident waves with respect to the proposed NSCP as well as NACP. Periodic boundary conditions (PBC) were employed for both x and y directions and perfectly matched layer (PML) boundary condition was employed in z direction. In the simulation, the permittivity of Ag, SiO_2 and H_2O is set as $\varepsilon_A = -11.75 + 0.37i$ [33], $\varepsilon_S = 2.13$ and $\varepsilon_H = 1.79$ at λ_0, respectively. The simulation domain (FDTD region) size was set as $2.1 \times 2.1 \times 2\ \mu m^3$. The Mesh region was applied in the regions where SPs exist. This region contain some finer meshes with small cubes of $2 \times 2 \times 2\ nm^3$ while a coarse meshing was set elsewhere. By employing the Frequency-domain field and power monitors in the software, the distributions of the electric field at $y = 0$ nm and $z = 115$ nm were investigated.

The distribution of the electric field of NACP/NSCP at different planes is shown in Fig. 2. Figures 2(a) and 2(b) show the magnitude of electric field at plane $y = 0$ near the gap between Ag films, respectively and the color scale bar shows the electric field intensity. We can see clearly that the standing wave (SW) pattern of SPs are formed in the gap for both platforms and the period of the SW-SPs is smaller when the gap is filled with water. The intensity of SW-SPs is more uniform in water cavity in comparison with that in air cavity. This phenomenon can be explained by the different propagation length of SPs in different medium. The propagation length of SPs is calculated to be 5.7 μm, which is much longer than that in air, i.e. 2.04 μm. This means that the absorptivity of the SPs in water is much higher than that in air. Therefore, the intensity of SPs in NSCP is stronger than that in NASP. As for the subtle difference in the uniformity of electric field intensity distribution, it can be attributed to the difference in refractive index. Since the refractive index difference between water and SiO_2 is smaller than that between air and SiO_2, the electric field distribution in NSCP is more uniform than that in NASP. One can apply this difference in different imaging applications. For instance, NASP can be applied for those imaging applications that require stronger intensity but with lower resolution, while NSCP can be applied for those imaging applications that require higher resolution but with relative weaker intensity. The magnitude of the electric field along vertical dashed lines in Figs. 2(a) and 2(b) is shown in Fig. 2(c). From this figure, it is found the intensity of electric field is increased abruptly at the Ag and water/air interface ($z = 100$ nm) due to SPs are excited and generated at this interface. The electric field is enhanced for about more than four times than that of the incident light and almost unchanged in the nano-cavity. Since the nano-cavity functions as a cavity resonator for SPs, this can be attributed to the Fabry-Perot resonance. This phenomenon was also reported elsewhere [34,35]. This enhanced and unchanged electric field is beneficial to the imaging of the immersed fluorescent or biological samples in the nano-cavity.

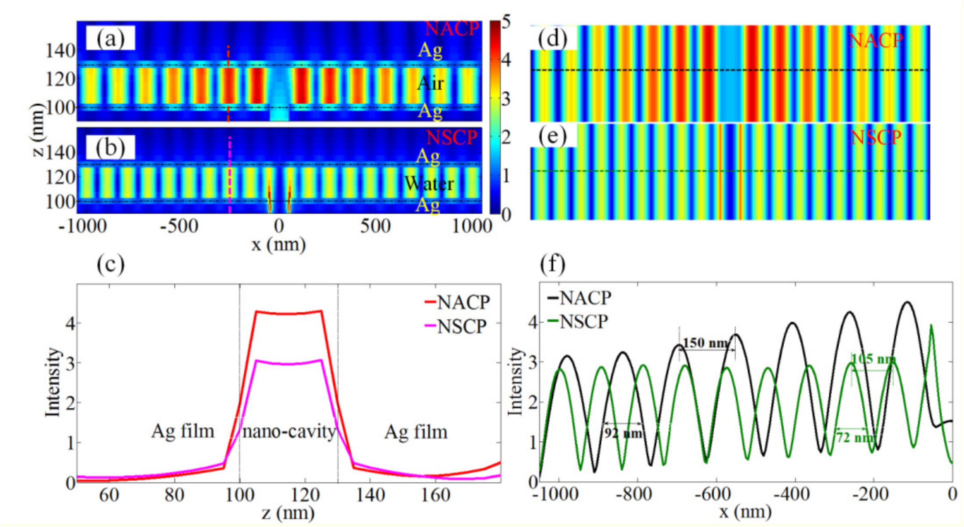

Fig. 2. The distribution of the SW-SPs in the nano-cavity of the NCP. (a) and (b) the distribution of *x*-component of the electric field in $y = 0$ plane for NACP and NSCP, respectively. (c) The intensity of the electric field along the vertical dashed lines in (a) and (b): red for (a) and magenta for (b). (d) and (e) the distribution of *x*-component of the electric field in $z = 115$ nm plane for NACP and NSCP, respectively. (f) The distribution of the electrical field intensity along the dashed lines, black for (d) and green for (e), respectively.

The distribution of the magnitude of electric field for both NCPs at plane $z = 115$ nm (the middle interface of the nano-cavity) is shown in Figs. 2(d) and 2(e), respectively. The electric field intensity distribution along the black dashed line in Fig. 2(d) and green in Fig. 2(e) was extracted and shown in Fig. 2(f), respectively. Because of the symmetry of the structure, only half of the lines are plotted. The period of the SW interference pattern of NSCP (the green line) is calculated to be only about 105 nm, which is only about 0.2 of the wavelength of the incident light, and the full width at half maximum (FWHM) is about 72 nm. However, for NACP, the period of the pattern is larger, i.e. 150 nm, with a 92 nm FWHM (the black line). Therefore, by simply changing the material of the solvent in nano-cavity, one can tune the period of the SW interference pattern in the object plane.

3. Analytical computation of the NCP model

In order to further understand the physical mechanism of the NCP, the wavevector of SPs supported by the NCP was analytically derived. For this purpose, the NCP model is simplified into a four-layer structure. The analytical computing structure and the permittivity of the material in each layer are shown in Fig. 3. Since a TM polarized plane wave incidents along z axis, it is hypothesized that SPs are already excited at the interface of Layer B and Layer C. From the Maxwell equation, the component of the electric and magnetic fields can be acquired. Considering the boundary conditions at the interface, i.e. the *x*-component of the electric field and the *y*-component of the magnetic field are continuous, one can get the following equations:

$$\alpha = \frac{k_{2z} / \varepsilon_2 + k_{1z} / \varepsilon_1}{k_{2z} / \varepsilon_2 - k_{1z} / \varepsilon_1} \tag{1}$$

$$\beta = e^{-2k_{3z}(d_2+d_3)} \frac{-(k_{4z} / \varepsilon_4 - k_{3z} / \varepsilon_3)}{k_{4z} / \varepsilon_4 + k_{3z} / \varepsilon_3} \tag{2}$$

$$\alpha e^{2k_{2z}d_2} = \frac{\beta*(k_{2z}/\varepsilon_2 + k_{3z}/\varepsilon_3)e^{2k_{3z}d_2} + k_{2z}/\varepsilon_2 - k_{3z}/\varepsilon_3}{\beta*(k_{2z}/\varepsilon_2 - k_{3z}/\varepsilon_3)e^{2k_{3z}d_2} + k_{2z}/\varepsilon_2 + k_{3z}/\varepsilon_3} \tag{3}$$

In above equations,

$$k_{iz} = \sqrt{\kappa^2 - k_0^2\varepsilon_i}\ (i = 1-4) \tag{4}$$

where k_{iz} and κ stand for the perpendicular and parallel components of the wavevector of SPs in the *ith* layer of NCP, respectively. k_0 represents the wavevector of the incident plane wave and d_i (i = 1-4) stands for the thickness of the *ith* film.

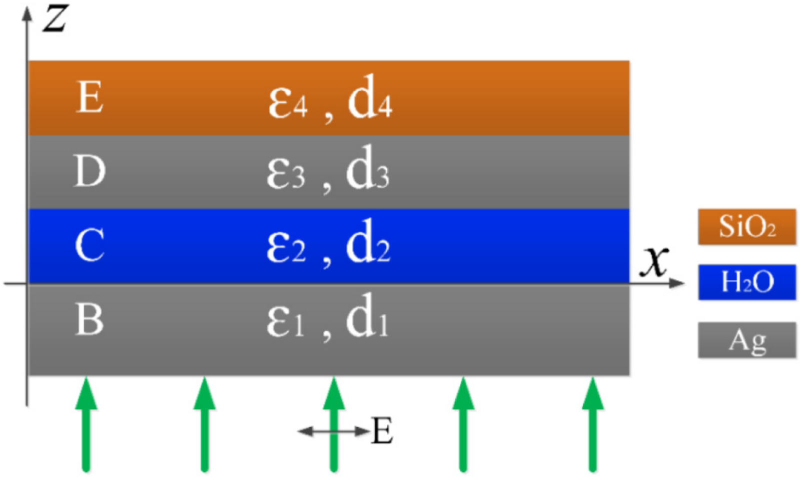

Fig. 3. The schematic diagram of the model of NCP used in analytic method. ε_i and d_i stand for the permittivity and thickness of the material in each layer.

4. The tunability of the period of SW-SPs pattern in NCP

After using above Eqs. (1)-(4), the wavevector of SPs in the NACP/NSCP were calculated and then compared with that of numerical results. For NACP, a wavevector β = 0.02 rad/nm of SPs was calculated, which corresponds to a plasmonic wavelength of 314 nm. Therefore, the period of the SW pattern is half of it, i.e. 157 nm (Fig. 4(b), Point A), which is a little bit larger than 150 nm obtained by the numerical simulation (Point A'). For NSCP, the period of SW-SPs was calculated to be 113 nm (Point B), which is again a little bit larger than the numerical result, i.e. 105 nm (Point B'). However, these values are in good agreement in general. Consequently, the validity of the NCP is verified by both numerical and analytical methods.

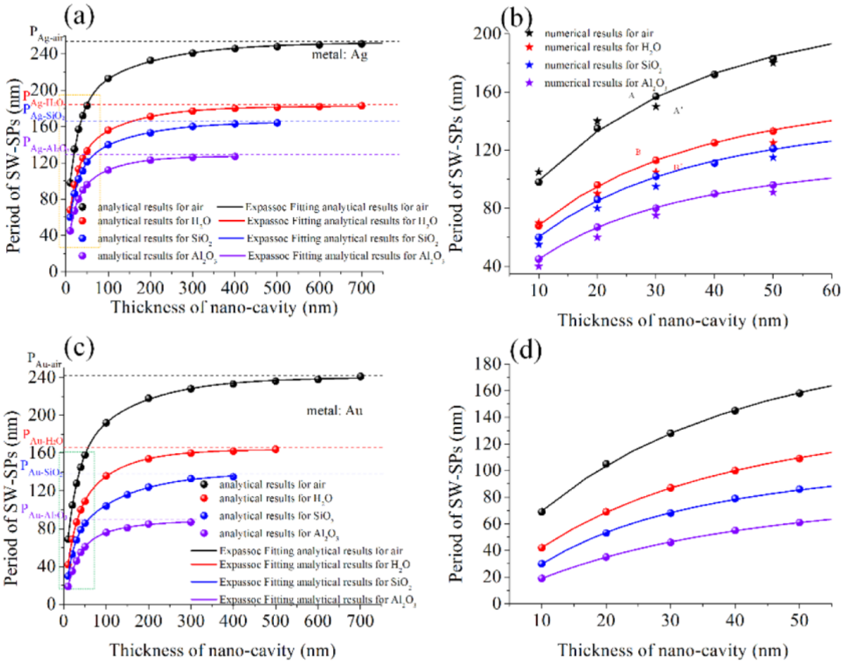

Fig. 4. The period of SW-SPs as a function of the thickness of nano-cavity. (a) The results for different dielectric material in nano-cavity of NCP, when the metal in NCP is Ag; (b) Details of the yellow dashed rectangle in (a). (c) The results for different dielectric material in nano-cavity of NCP, when the metal in NCP is Au; (d) Details of the green dashed rectangle in (c).

To show the tunability of the NCP model, the effects of different parameters, such as the thickness and material of nano-cavity on the period of SW-SPs were analyzed and the results are shown in Fig. 4. As shown in Fig. 4, in general, the period of SW-SPs increases with the thickness of nano-cavity in an ExpAssoc expression. Figures 4(b) and 4(d) show the details of comparison between analytical and numerical results in Fig. 4(a) (the orange dashed rectangle) and Fig. 4(c) (the green dashed rectangle), respectively. From Fig. 4(b), it can be found that when the dielectric material in nano-cavity is changed to SiO_2 or Al_2O_3, the analytical results also agree with the numerical ones very well. For the metal material of the NCP is Ag, depicted in Fig. 4(a), the period of SW-SPs is almost the same when the thickness is larger than 400 nm. In this case, the period SW-SPs in NACP is close to that of the period of the simple Ag/air interface ($P_{Ag\text{-}air}$ = 254 nm) and for NSCP the period is close to $P_{Ag\text{-}H2O}$ (183 nm). And this phenomenon can also be seen in Fig. 4(c), where the metal is changed to Au. This can be explained by the analytical methods. From Eqs. (2) and (3), one can find that if the d_2 is larger enough, such as 500 nm, then α or β almost equals to zero. Equation (1) is changed to Eq. (5),

$$k_{2z} / \varepsilon_2 + k_{1z} / \varepsilon_1 = 0 \tag{5}$$

By combing Eqs. (4) and (5), one can get Eq. (6),

$$\kappa = k_0 \sqrt{\frac{\varepsilon_1 \varepsilon_2}{\varepsilon_1 + \varepsilon_2}} \tag{6}$$

It can be found that Eq. (6) gives the wavevector of SPs exited in the simple metal/dielectric interface. Therefore, when the thickness of nano-cavity is smaller than 200 nm, the NCP can be used to achieve SPs with a higher wave-vector. In another word, the dynamic range of the thickness of nano-cavity of NCP is about 200 nm, which is more suitable for the imaging of cell membrane, fluorescent, etc.

When compared four lines in Figs. 4(a) and 4(c), it can also be seen that when the material in nano-cavity was changed from air to Al_2O_3, the period of SW-SPs decreased. Therefore, the higher the permittivity of dielectric material in the nano-cavity, the smaller the period of SW interference pattern. Moreover, it is found that when changing the metal material of NCP from Ag to Au, the period of SW-SPs decreases significantly. However, since the propagation length of SPs in Au is much smaller than that in Ag [36]. Ag is preferred in NCP model. It should also be noted that the propagation length of SPs can also be extended by designing special metasurfaces such as directional surface plasmonic excitation [37–39]. Therefore, one can use metals in NCP with both small real and imaginary parts of the permittivity to further increase the wavevector of SPs. Effective materials with the desired permittivity by mixing or doping dielectrics or semiconductors in metallic films can also be used [40].

5. The verification of the effectiveness of the NCP in fluorescent imaging

It is necessary to prove whether the fluorescent signals can penetrate the upper Ag film with a thickness of 50 nm or not if one want to NCP for optical imaging. For this purpose, a model shown in Fig. 5(a) is built to test the propagation of the fluorescent signals excited by surface plasmonic wave inside the nano-cavity of NCP. In this model, a dipole, placed in the nano-cavity, was used to simulate point source radiator, such as the radiation from a fluorescent molecule [41,42]. In order to demonstrate the results clearly, the amplitude of the dipole was set as 10 and frequency-domain field and power monitor was set at the plane which is 10 nm away from the top silica substrate of NCP.

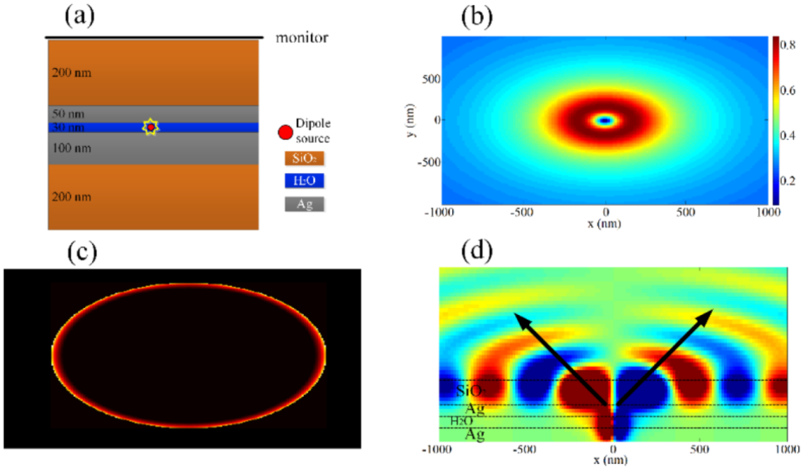

Fig. 5. The verified results of NCP used in fluorescent imaging. (a) The schematic diagram of the verified model. (b) The distribution of electric field at the plane 10 nm above the upper SiO_2 film. (c) The SPCE intensity in the far field after near to far field projections. (d) The electric field from the dipole source at the $y = 0$ plane.

Figure 5(b) shows the distribution of electric field at the plane 10 nm above the upper SiO_2 film. This electric field is the near-field distribution of the dipole source. The near to far field projection in FDTD software was used to calculate the electromagnetic fields in the far field. Figure 5(c) shows the result of near to far field projections. Surface Plasmon-Coupled Directional Emission (SPCE) light intensity distribution can be clearly seen in the figure. Figure 5(d) shows electric field distribution of the dipole source at $y = 0$ plane. It is indicated in the figure that the electric field is highly directed in the SiO_2 film and the air (see the black arrow). However, the electric field radiation is blocked by the lower Ag film due to its large thickness. This phenomenon is similar to the Fig. 2 in [41]. Consequently, the fluorescent signal excited from the nano-cavity can penetrate through the upper Ag and SiO_2 films in a SPCE form so that it can be detected in free space.

6. The imaging results when NSCP used in PSIM

The proposed NSCP was applied in wide-field super-resolution imaging in a PSIM mode. Figure 6(a) shows the schematic diagram of the process of NSCP-PSIM imaging. In order to exhibit its capability in the resolution improvement, the image of some point objects (POs) were tested. The POs were deposited in the water nano-cavity. Actually, NSCP can be integrated with nano-fluidic system so that objects to be observed can be passed into the nano-cavity in real time. The SW-SPs interference pattern shown in Fig. 6(a) is used to illuminate the POs and then the surface plasmon-coupled emission (SPCE) signals of the POs can be recorded in far field. The phase shift of SPs can be obtained simply by changing the incident angle θ [20, 21, 43] as shown in Fig. 6(b). For different incident angles, the excited SPs has a different phase so that the interference pattern of the SW-SPs has a different phase change for different incident angle. This relationship between the SPs phase shift and the incident angle was clearly shown in Fig. 6(b). When the incident angle changes from 0, 4 to 8.5°, the interference pattern shows 120° mutual phase difference along the lateral direction. However, when the incident angle becomes larger than 8.5°, the interference pattern of the SW-SPs starts to deteriorate so that the imaging quality will be affected [43]. To realize a resolution enhanced image, the same method in our previous work is taken and the details can be found elsewhere [26]. The numerical post-processing method used to reconstruct the high-resolution image is the same as that used in standing-wave total internal reflection fluorescence [44].

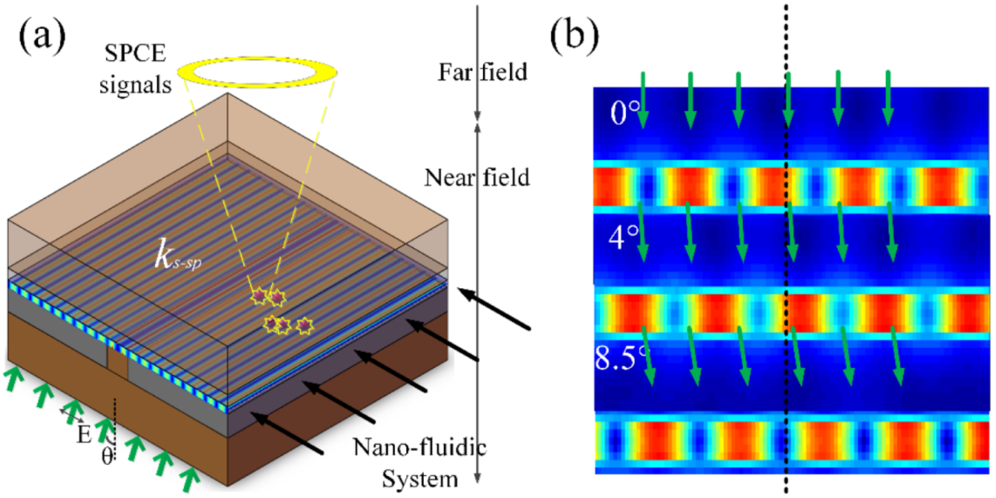

Fig. 6. The schematic diagram of the NCP used in PSIM. (a) Optical configuration of SPs generated by NCP. The plasmonic interference pattern is generated by two adjacent counter propagating SPs and used to excite the quantum dots in nano-cavity, and (b) schematic demonstration of 120° phase shift of the SPs interference pattern with different incident angles (0, 4, and 8.5°).

In our numerical model, POs with a size of 10 nm and a 600 nm emission wavelength were placed randomly in nano-cavity to demonstrate the imaging performance of the NSCP. An immersion oil objective with NA = 1.42, is used to detect the fluorescent signal from the POs. The simulation results are shown in Figs. 7(a)-7(d). Figure 7(a) shows the reconstructed image of the POs by NSCP used in PSIM with an incident wavelength of 532 nm. Figure 7(b) shows the image of POs by using a conventional homogeneous illumination. Comparing these two pictures, one can find that the significant resolution improvement in NSCP has been obtained. Figure 7(c) shows a comparison of the PSF profile across the red and black dash lines in Figs. 7(a) and 7(b), respectively. As shown in Fig. 7(c), the FWHM of the PSF of the conventional epi-fluorescence microscopy (black line) is about 218 nm. However, the FWHM is about 83 nm for PSIM using the NSCP, which means that the imaging resolution improvement is about 2.63 folds. The PO is 10 nm along *x* direction. The PSF of two closely placed POs marked by magenta and green dashed dot lines in Figs. 7(a) and 7(b) is shown in Fig. 7(d). The true distribution of these two POs also depicted as black rectangles in Fig. 7 (d). From this figure, it can be seen that the POs separated by 65 nm can be resolved by NSCP-PSIM but cannot be resolved by a conventional homogeneous illumination. Figure 7(e) shows the cross sectional profile image of two point POs at different separation distances by using NSCP-PSIM. Based on the Rayleigh criterion, it is shown that NSCP-PSIM has the capability to resolve objects separated by about 60 nm. Figure 7(e) shows the image of two POs with 60 nm separations. However, from Figs. 7(a), 7(b) and 7(e), there exist sidelobes surrounding the centrals and these artifacts can be eliminated by using appropriate deconvolution algorithm to further improve the image quality [45–47].

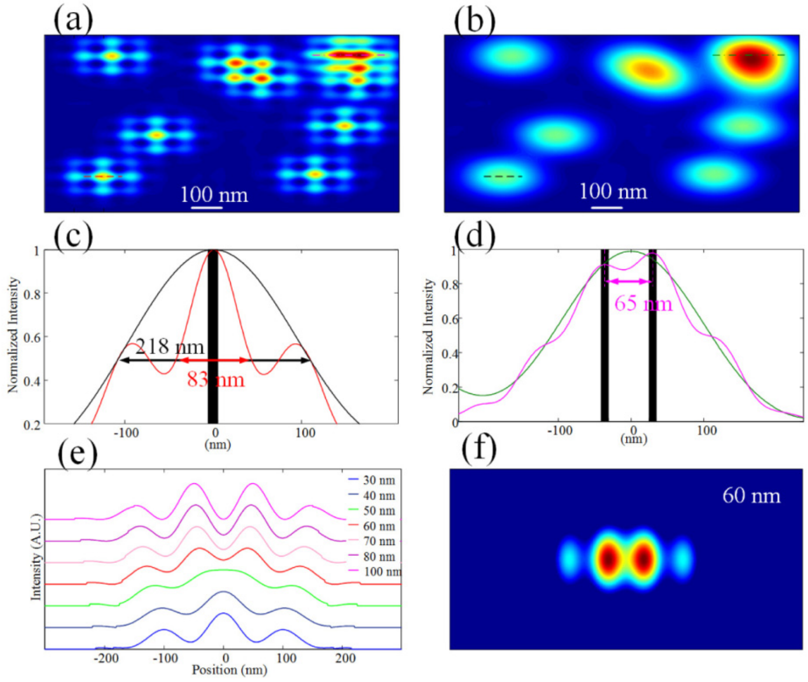

Fig. 7. The simulation results of the NCP imaging performance. (a) A reconstructed image; (b) A diffraction-limited image; (c) FWHM comparison between conventional epi-fluorescence microscopic image (black curve) and the super-resolution image by using the NCP (red line) in PSIM; (d) The intensity of the imaging of two POs along the dot dashed lines in (a) and (b): magenta for (a) and green for (b). The black rectangles in (c) and (d) represent the true distribution of PO. (e) Simulated composite images for NCP-PSIM imaging of two separated by 30, 40, 50, 60, 70, 80, and 100 nm in *x*-direction; (f) The reconstructed image of two POs separated by 60 nm.

7. Conclusions

In summary, a nano-cavity platform (NCP) used in super-resolution microscopy was demonstrated in this work. This new platform features a nano-cavity that can be integrated with the nano-fluidic system. NCP is simple and elegant but still can support SPs wave with a higher wavevector. The ability of the NCP to support short wavelength SPs was proved by employing both rigorous numerical and analytical methods. Additionally, the period of the plasmonic interference pattern can be easily tuned by varying the parameters of the nano-cavity in NCP. It is found that the period of the SPs interference pattern is only about 0.2 of the wavelength of the incident light. The effectiveness of the NCP in fluorescent imaging and the imaging results of this NCP applied in PSIM were also discussed. The numerical results demonstrate that the reconstructed quantum dots image shows a 2.63-fold improvement on the resolution in comparison with that of the conventional epi-fluorescence microscopy. All of these advantages of NCP promise great potential applications in the field of high-speed, real-timely super-resolution biomedical imaging.

Funding

National Science Foundation of China (NSFC) (61361166004, 61475156) and Technology Department of Jilin Province (20140519002JH).